ACS APPLIED MATERIALS & INTERFACES

Research Article

www.acsami.org

Enhanced Photovoltaic Properties and Long-Term Stability in Plasmonic Dye-Sensitized Solar Cells via Noncorrosive Redox Mediator

Heesuk Jung,[†,‡] Bonkee Koo,[†,‡,§] Jae-Yup Kim,[‡] Taehee Kim,[‡] Hae Jung Son,[‡] BongSoo Kim,[‡,⊥] Jin Young Kim,[‡,⊥] Doh-Kwon Lee,[‡] Honggon Kim,[‡,⊥] Jinhan Cho,[§] and Min Jae Ko*[,‡,⊥]

[‡]Photo-Electronic Hybrids Research Center, Korea Institute of Science and Technology (KIST), Seoul 136-791, Korea

[§]Department of Chemical and Biological Engineering, Korea University, Anam-dong, Seongbuk-gu, Seoul 136-713, Korea

[⊥]Green School, Korea University, 145, Anam-ro, Seongbuk-gu, Seoul 136-701, Korea

Supporting Information

ABSTRACT: We demonstrate the localized surface plasmon resonance (LSPR) effect, which can enhance the photovoltaic properties of dye-sensitized solar cells (DSSCs), and the long-term stability of size-controlled plasmonic structures using a noncorrosive redox mediator. Gold nanoparticles (Au NPs) were synthesized with a phase transfer method based on ligand exchange. This synthetic method is advantageous because the uniformly sized Au NPs, can be mass produced and easily applied to DSSC photoanodes. The plasmonic DSSCs showed an 11% improvement of power conversion efficiency due to the incorporation of 0.07 wt % Au NPs, compared to the reference DSSCs without Au NPs. The improved efficiency was primarily due to the enhanced photocurrent generation by LSPR effect. With the cobalt redox mediator, the long-term stability of the plasmonic structures also significantly increased. The plasmonic DSSCs with cobalt(II/III) tris(2,2′-bipyridine) ($[Co(bpy)_3]^{2+/3+}$) redox mediator maintained the LSPR effect with stable photovoltaic performance for 1000 h. This is, to our knowledge, the first demonstration of the long-term stability of plasmonic nanostructures in plasmonic DSSCs based on liquid electrolytes. As a result, the enhanced long-term stability of plasmonic NPs via a noncorrosive redox mediator will increase the feasibility of plasmonic DSSCs.

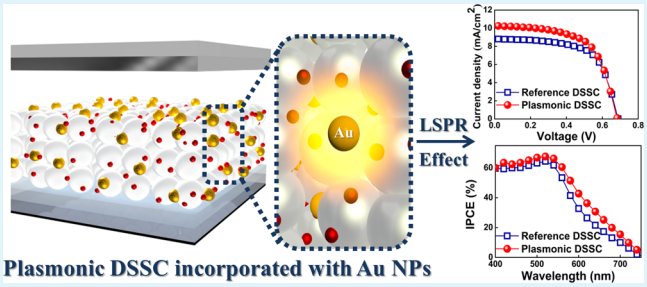

KEYWORDS: *dye-sensitized solar cells, gold nanoparticles, localized surface plasmon resonance, corrosion, cobalt-based electrolyte, long-term stability*

INTRODUCTION

The optical properties of noble metal NPs have attracted considerable attention since Faraday's study of colloidal Au NPs.[1] The unique properties of noble metal NPs are result of the localized surface plasmon resonance (LSPR) phenomenon. The LSPR phenomenon is based on the collective oscillations of electrons, called surface plasmons, and can be manifested by the constructive interference between electromagnetic light fields and surface plasmons of metal NPs.[2−6] This LSPR effect amplifies intense electromagnetic fields near the metal NPs, leading to the precise control of optical fields and the enhanced absorption band in UV−vis spectrum.[7] The LSPR effect has been applied to wide range of applications in surface-enhanced spectroscopy,[8−10] optical antennas,[11] photolithography,[12] photocatalysts,[13−15] and other applications.[16,17]

In particular, plasmonic nanostructures have been applied in a variety of solar cell types to enhance the photovoltaic performance. The enhanced light absorption through LSPR effects could maintain the optical absorption, while reducing the physical thickness of solar cell absorption layers.[18] Schaadt et al. reported an 80% enhancement of absorption by Au NP depositions on silicon (Si) solar cells.[19] Derkaces et al. deposited Au NPs on amorphous Si solar cells and achieved an increase in efficiency via the excitation of surface plasmon resonances.[20] Pillai et al. achieved a 33% increase in the photocurrent for thin Si-on-insulator (SOI) cells depositing silver (Ag) NPs on the devices.[21] A significant enhancement of the photocurrent in n-CdSe/p-Si heterostructures was also reported by Konda et al. because of surface plasmon excitations via Au NPs on the surfaces of heterojunction diodes.[22] Wu et al. demonstrated that the conversion efficiency of bulk heterojunction polymer solar cells could be improved by local electromagnetic fields near Au NPs.[23] Wang et al. also reported plasmonic effects on organic bulk heterojunction solar cells with Ag NPs and achieved a 13% improvement in the conversion efficiency.[24]

Received: August 4, 2014
Accepted: October 8, 2014
Published: October 8, 2014

In the case of dye-sensitized solar cells (DSSCs), Ihara et al. proved an enhanced absorption coefficient of the Ru-dye using an Ag island film.[25] Jeong et al. investigated the photocurrent improvement due to the increased effective absorption cross-section of the dye as a result of the neighboring Ag NPs.[26] More recently, various plasmonic structures have been used to increase the photovoltaic performance of DSSCs.[27−30]

In spite of the significant photovoltaic performance improvements, plasmonic DSSCs are limited by the stability of noble metal NPs. Direct contact with the I^-/I_3^--based liquid electrolyte causes corrosion of the metal NPs. Several techniques have been attempted to resolve the dissolution problem of metal NPs in plasmonic DSSCs. Atomic layer deposition (ALD) of metal oxides has been used to create a thin coating on the metal NPs to prevent corrosion.[31,32] Alternately, the application of core−shell NPs such as Au@TiO_2 and Au@SiO_2 can be used to avoid dissolution of the metal. The shell layers have preserved core metal NPs from I^-/I_3^- redox electrolyte and showed enhanced photocurrent generation by LSPR effect on DSSCs.[33,34] Although these methods created a shell to avoid direct contact with the I^-/I_3^- redox couple, the metal NPs could be still dissolved by the permeation of I^-/I_3^- ions through the thin coating shell.[35] A thick coating layer is necessary for enhanced stability; however, thick coating layers cannot be applied to metal NPs because the LSPR effect on the light absorption of dye strongly depends on the distance from the NPs.[26,36,37] The amplified electric fields dramatically decrease with the distance from the metal NPs. Therefore, to overcome these coating method difficulties, it is necessary to consider alternatives to the conventional I^-/I_3^- redox mediator. Various redox couples have been investigated as alternative electrolytes in DSSCs.[38−43] Among the diverse redox mediator candidates, cobalt complexes are promising because of their weak visible-light absorption and potential for high efficiency.[44,45]

In this study, we used the cobalt(II/III) tris(2,2′-bipyridine) ($[Co(bpy)_3]^{2+/3+}$) redox couple for enhanced long-term stability of Au NPs without sacrificing the plasmonic effects on the DSSCs. The Au nanostructure corrosion could be eliminated by applying cobalt-based electrolytes in plasmonic DSSCs. In addition, we synthesized the 4-dimethylaminopyridine (DMAP)-capped Au NPs using a modified two-phase transfer method and incorporated these plasmonic structures into the TiO_2 photoanodes.[46] Synthesis methods based on two-phase transfer have the advantage of mass producing Au NPs with high uniformity in the particle size, and easy application in TiO_2 paste. Through the application of size-controlled Au NPs with DMAP stabilizer and cobalt redox mediator, we could verify the enhanced photovoltaic performance of DSSCs by the LSPR effect and the resulting long-term stability of the plasmonic structures.

RESULTS AND DISCUSSION

Synthesis and Characterization of Au Nanostructures. The Au NPs were synthesized using a phase transfer method based on the ligand exchange process as presented in Scheme 1. When the Au NP synthesis is performed in aqueous media, it is difficult to obtain concentrated NPs or precisely control the particle size. On the contrary, Au NPs with a narrow size distribution as well as higher concentration can be obtained from synthesis in organic solvents.[46] Therefore, we synthesized Au NPs in toluene using tetraoctylammonium bromide (TOABr) as a ligand for mass produced uniformly sized NPs.

Scheme 1. Synthesis of Au NPs Based on Phase Transfer from Toluene to DI Water by the Addition of DMAP Stabilizers

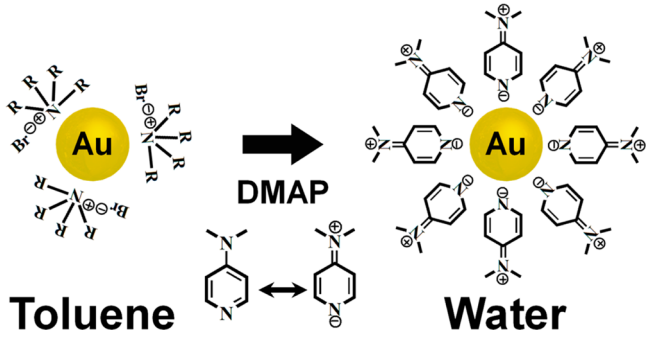

After the synthesis, the TOABr-capped Au NPs were transferred to an aqueous solution by ligand exchange between TOABr and DMAP. Due to the DMAP stabilizer, the size-controlled Au NPs were easy to blend with TiO_2 paste for plasmonic photoanode fabrication. Figure 1a and b show the high-resolution transmission electron microscopy (HR-TEM) images of Au NPs with different stabilizers. As shown in Figure 1a, the diameter of TOABr capped Au NPs is about 5 nm, and the particle size is very uniform. The inset of Figure 1a illustrates the complete transfer of the Au NPs from toluene to deionized (DI) water. The addition of a DMAP solution (0.1 M) to the TOABr-Au mixtures led to ligand exchange across the toluene/water interface. The endocyclic nitrogen atoms of the DMAP molecules formed a complex with the surface atoms of the Au NPs, and the partial protonation of exocyclic nitrogen atoms resulted in the Au NP transfer into DI water.[47] Figure 1b proves the successful phase transfer of the Au NPs from toluene to DI water. The uniformity of the DMAP-stabilized Au NPs is high with no significant aggregation. The inset to Figure 1b also shows the DMAP-capped Au NPs with 5 nm size, and the lattice distance (d) is 0.24 nm relevant to the (111) plane of Au.

To confirm the crystallinity of DMAP-capped Au NPs, the X-ray diffraction (XRD) pattern was measured at 2θ ranging in the 30 to 90° range for the Au NPs deposited on the SiO_2 substrate. As shown in Figure 1c, the XRD pattern showed two distinct peaks, which can be assigned to the diffraction of the (111) and (200) planes of the face-centered cubic (FCC) Au NPs. We also observed the UV−vis spectra of the Au NPs in solution with different ligands to substantiate the successful transfer of the Au NPs from toluene to DI water. Figure 1d illustrates the plasmonic absorption peak position of TOABr-capped Au at 530 nm. The DMAP-capped Au NPs show a broadening absorption band at 531 nm, and the observed broadening is due to flocculated particles. As the pH value of the DMAP solution was lowered, the ratio of flocculated particles increased.[48] However, the flocculation of particles could be easily suppressed by sonication, and the colloidal particles were stable in the pH range from 7 to 12. These data demonstrate that synthesis based on the phase transfer method could yield size-controlled Au NPs with a high concentration and crystallinity in an aqueous solution.

Chemical Stability of Au NPs in Electrolytes. Previous studies have reported that the I^-/I_3^- redox couple could dissolve metal NPs such as Ag and Au NPs. Due to this corrosion problem, many studies proposed coating the metal NPs via atomic layer deposition (ALD) method or the

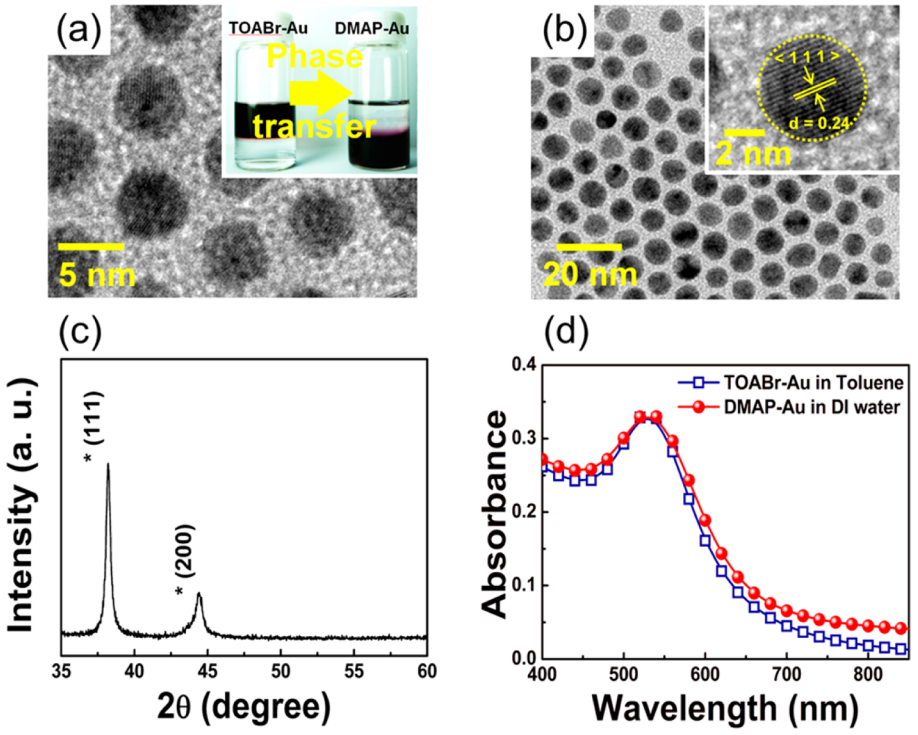

Figure 1. Synthesis and characterization of Au NPs. (a) TEM image of TOABr Au NPs synthesized in toluene. The inset shows the phase transfer of the Au NPs from toluene to DI water. (b) Au NPs after transfer into an aqueous solution by the addition of DMAP. The inset shows 5 nm Au NPs and the lattice distance relevant to (111) plane of Au. (c) XRD patterns of Au NPs stabilized by DMAP (d) Absorbance spectra of TOABr-capped Au NPs in toluene (blue line) and DMAP-capped Au NPs in a DI solution (red line).

synthesis of metal core@nonmetal shell NPs.[26,31−35,49] Nevertheless, I^-/I_3^- ions could penetrate the thin coating layers within a very short time frame.[26,35] In order to avoid corrosion of the Au NPs, we synthesized and utilized cobalt(II) and (III) complexes as an alternative electrolyte for developing plasmonic DSSCs. To investigate the chemical stability of the Au NPs, we measured the time-dependent absorption spectra of the DMAP-capped Au NPs in solution after adding two types of electrolytes. As shown in Figure 2a, the plasmonic absorption peak of the Au solution rapidly decreases after the addition of the I^-/I_3^- redox electrolyte, and the peak seems to disappear within 8 min. The extinction of this absorption peak is ascribed to the fact that the I^-/I_3^- redox couple effectively oxidized the Au NPs to form a thermodynamically stable $[AuI_2]^-$ complex by the following reaction[50]

$$2Au + I_3^- + I^- \Leftrightarrow 2[AuI_2]^- \quad (1)$$

On the contrary, Figure 2b shows that there is no discernible difference in the absorption peak of the Au solution with $[Co(bpy)_3]^{2+/3+}$ redox couple after 12 h, implying that the DMAP-capped Au NPs would not corrode in $[Co(bpy)_3]^{2+/3+}$ based electrolytes. This obvious distinction of the time-dependent absorption peaks between $[Co(bpy)_3]^{2+/3+}$ and I^-/I_3^- redox couple verifies the long-term stability of Au nanostructures with cobalt redox electrolytes.

We also measured the cyclic voltammograms to investigate the electrochemical behaviors of Au NPs in electrolytes based on $[Co(bpy)_3]^{2+/3+}$ and I^-/I_3^-. In Figure 3a, the cyclic voltammograms exhibit two redox peaks at E_{ox} (0.24 V) and E_{red} (−1.5 V) for Au-coated FTO electrodes in I^-/I_3^- redox electrolytes, measured at a scan rate of 25 mV/s. These peaks are attributed to effect of I^-/I_3^- redox couples on Au atoms according to the following electrochemical reaction[51]

$$Au + 2I^- \rightarrow AuI_2^- + e^- \quad (2)$$

$$I_3^- + 2e^- \rightarrow 3I^- \quad (3)$$

The currents of E_{ox} and E_{red} for the Au films significantly decrease with the number of cycling tests, indicating that the electrochemical response attenuates through the dissolution phenomena of Au atoms. As the thermodynamically stable AuI_2^- complexes were formed, the amount of pristine Au atoms decreased, and I_3^- could not be reduced to I^-. Thus, the rate of oxidation and reduction became drastically slower according to the cycling number. The inset of Figure 3a also indicates corrosion of the Au atoms on FTO by the I^-/I_3 redox couple. As the cycle number increases, the absolute currents for oxidation and reduction were dramatically reduced.

As shown in Figure 3b, the cyclic voltammograms exhibit two redox peaks at E_{ox} (0.24 V) and E_{red} (−0.08 V) for Au electrodes with cobalt complex redox electrolytes, measured at a scan rate of 25 mV/s. The Au-coated electrodes exhibited reversible and ideally shaped CVs during 1500 cycles, which agrees with the previously reported study.[44] This result suggests that no observable dissolution phenomena of the Au atoms existed and that the Au NPs have a stable electrochemical activity with cobalt redox species. The inset of Figure 3b also shows the electrochemical stability of Au atoms with $[Co(bpy)_3]^{2+/3+}$ redox couple. The absolute currents for oxidation and reduction were preserved for 1500 cycles. From these results, we confirm that the electrochemical behavior of Au atoms is stable in cobalt redox electrolytes, compared with those of conventional electrolyte based on I^-/I_3^-.

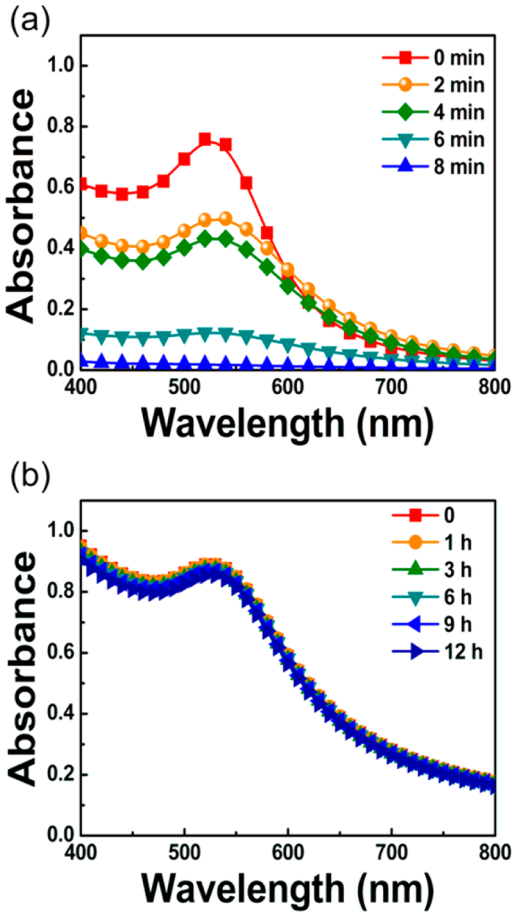

Figure 2. Time-dependent UV−vis absorbance spectra of DMAP-Au solution after adding (a) the I^-/I_3^- redox electrolytes containing 0.1 M $LiClO_4$, 0.05 M LiI, 0.03 M I_2, 0.1 M GSCN and 0.5 M TBP in ACN or (b) the $[Co(bpy)_3]^{2+/3+}$ redox electrolytes containing 0.22 M $Co(bpy)_3(PF_6)_2$, 0.033 M $Co(bpy)_3(PF_6)_3$, 0.1 M $LiClO_4$ and 0.5 M TBP in ACN.

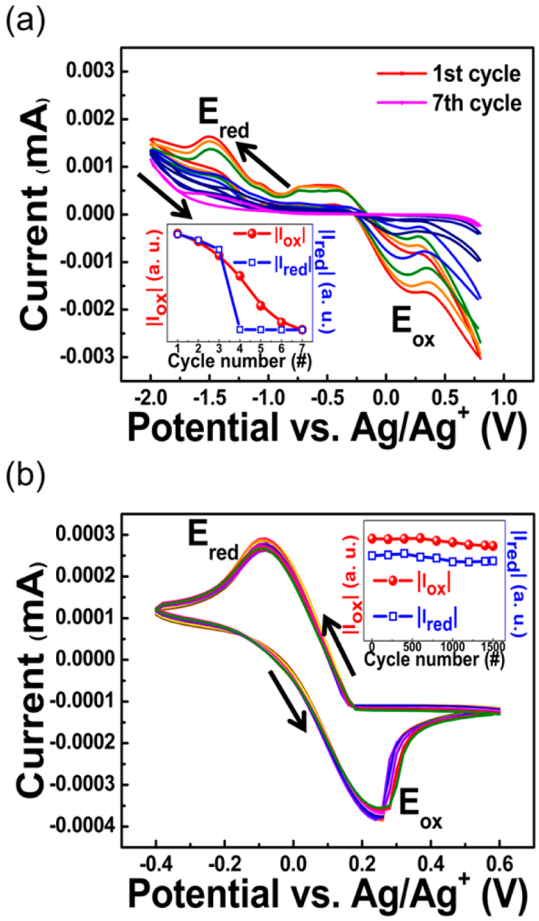

Figure 3. Cyclic voltammograms for $[Co(bpy)_3]^{2+/3+}$ and I^-/I_3^- redox mediators using Au NPs coated FTO as a working electrode, measured at a scan rate of 25 mV/s (a) The I^-/I_3^- redox electrolytes containing 0.1 M $LiClO_4$, 0.05 M LiI, 0.03 M I_2, 0.1 M GSCN and 0.5 M TBP in ACN. The inset shows the absolute currents of oxidation (I_{ox}) and reduction (I_{red}) with respect to the cycle number (b) The $[Co(bpy)_3]^{2+/3+}$ redox mediators containing 0.22 M $Co(bpy)_3(PF_6)_2$, 0.033 M $Co(bpy)_3(PF_6)_3$, 0.1 M $LiClO_4$ and 0.5 M TBP in ACN. The dependency of the absolute currents of oxidation (I_{ox}) and reduction (I_{red}) is also shown in the inset.

Effect of the Au NP Concentration on the Photovoltaic Performance of DSSCs. To investigate the optimum concentration of Au NPs in TiO_2 photoanodes, various amounts of Au NPs (Au to TiO_2 weight ratio from 0.03 to 0.1 wt %) were incorporated in the TiO_2 paste. Figure 4 shows the dependence of the photovoltaic parameters on the concentration of Au NPs. For reliable measurements, 20 parallel devices were fabricated at each condition. As shown in Figure 4a and b, the short circuit current density (J_{sc}) gradually increased without severe loss of the open circuit voltage (V_{oc}) as the concentration of Au NPs increased to 0.07 wt %. On the other hand, J_{sc} decreased when the concentration of Au NPs increased beyond 0.07 wt %. The fill factor (FF) and power conversion efficiency (η) also decreased noticeably when the concentration is greater than 0.07 wt %, as shown in Figure 4c and d, respectively. We conjecture that the degraded performance at these concentrations could be ascribed to the trapping of electrons as well as the loss of light absorption due to the excessive presence of Au NPs.[33,34] From these results, we could optimize the concentration of Au NPs in the photoanodes and maximize the LSPR effect for the enhanced light harvesting of DSSCs.

Enhanced Light Harvesting of Dyes by LSPR Effect. The LSPR phenomenon occurs when free electrons on the surface of nanostructures are stimulated by incident light. As the frequency of light matches with the natural frequency of collective oscillations of surface electrons, the electric fields around plasmonic NPs induce enhanced strength of the incident light.[52−55] This enhancement of the localized electromagnetic fields around nanostructures is a key factor for increasing the absorption cross-section of dyes. In order to validate the LSPR effect, 4 μm TiO_2 films with 0.07 wt % Au NPs were prepared. For comparison, pristine TiO_2 photoanodes with same thickness were prepared. In order to examine whether the amount of dye loading on the photoelectrodes would change after the introduction of Au NPs, we compared the dye loading amounts of the films, and similar amounts of dye loading on pristine and plasmonic photoanodes were evaluated. The obtained values are 2.65×10^{-7} mmol cm^{-2} and 2.63×10^{-7} mmol cm^{-2} for the pristine TiO_2 films and films with 0.07 wt % Au NPs, respectively. Therefore, the differences in the photovoltaic properties do not originate from the amount of dyes on the films.

The absorption spectra of different types of dye-adsorbed TiO_2 films are displayed in Figure 5. While the dyed pristine TiO_2 films and films incorporated Au NPs exhibit similar

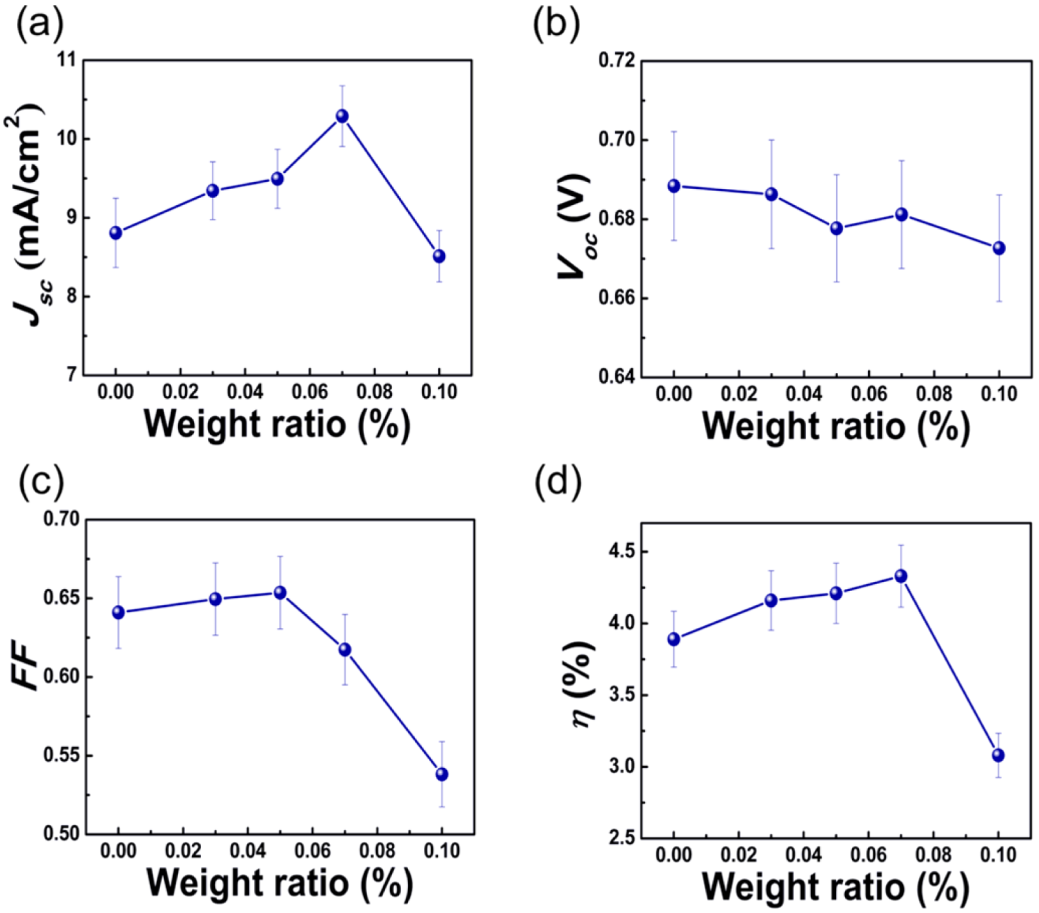

Figure 4. Dependence of photovoltaic parameters on the amounts of Au NPs in photoanodes: (a) short-circuit current density (J_{sc}), (b) open circuit voltage (V_{oc}), (c) fill factor (FF), and (d) efficiency (η).

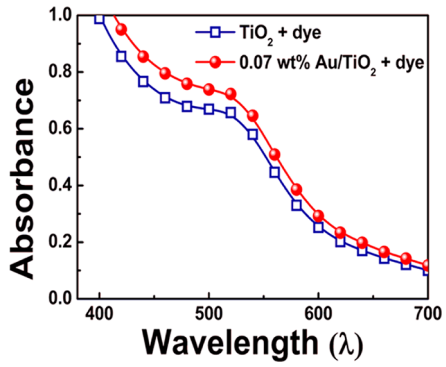

Figure 5. UV–vis absorbance spectra of the dye-adsorbed TiO_2 film (blue line) and dye-coated TiO_2 film with 0.07 wt % Au NPs (red line).

shapes of absorption spectra, we observe enhanced light absorption for films containing 0.07 wt % Au NPs. This is in good agreement with previous reports on the enhancement of the light harvesting efficiency by plasmonic effects.[25,26,30−35] The absorption cross-section of Z907 dye increased due to the strong coupling between the locally enhanced electromagnetic fields of Au NPs and the electronic transitions of the dye.[17] This enhanced light harvesting of dye was observed over the whole visible wavelength.[33]

LSPR Effect on Photovoltaic Performance of DSSCs. To investigate the LSPR effect on photovoltaic performance of DSSCs, reference cells with pristine TiO_2 films and plasmonic cells with photoanodes containing 0.07 wt % Au NPs were fabricated. Figure 6 shows the photocurrent density–voltage

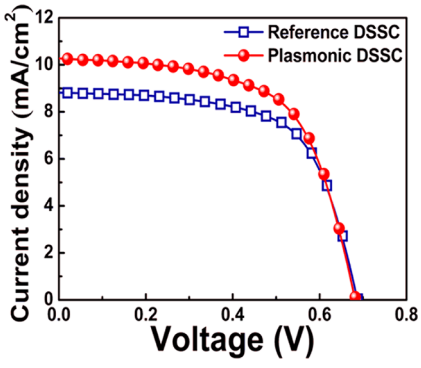

Figure 6. Photocurrent density–voltage (J–V) curves of reference DSSC with pristine TiO_2 photoanodes (blue line) and plasmonic DSSC with photoanodes containing 0.07 wt % Au NPs (red line).

characteristics (J–V curves) of the reference DSSCs and plasmonic DSSCs incorporated with 0.07 wt % Au NPs. The thickness of the TiO_2 photoanode films for both the reference and plasmonic cells was fixed at 4 μm. The photovoltaic parameters are summarized in Table 1. For statistical analysis, Histograms and standard deviations of photovoltaic properties of the reference DSSCs and plasmonic DSSCs with 0.07 wt % Au NPs are shown in Figure S1 and Table S1 in the Supporting Information, respectively. The plasmonic DSSCs exhibited an

dx.doi.org/10.1021/am5051982 | ACS Appl. Mater. Interfaces 2014, 6, 19191−19200

Table 1. Photovoltaic Parameters of Reference DSSC and Plasmonic DSSC with 0.07 wt % Au NP Incorporated Photoanode

samples[a]	J_{sc} (mA/cm^2)	V_{oc} (V)	FF	η (%)
reference	8.81	0.69	0.64	3.89
0.07 wt %	10.29	0.68	0.62	4.34

[a]The photoanodes thickness for reference and plasmonic DSSCs are adjusted 4 μm. The active area of films is 0.40 cm^2 and the black mask was applied to the surrounding active area during the measurement. The photovoltaic parameters were measured under AM 1.5 illumination (100 mW/cm^2).

enhanced η of 4.34%, compared to 3.89% of reference DSSCs. We find V_{oc} and FF of plasmonic DSSCs to be 0.68 V and 0.62, respectively. For the reference DSSCs, V_{oc} and FF are 0.69 V and 0.64, respectively. The V_{oc} could be affected by the types of cobalt complexes because of the various redox potentials. Feldt et al. reported that the redox potential of $[Co(bpy)_3]^{2+/3+}$ is less positive than that of cobalt(III/II) tris(5-nitro-1,10-phenanthroline), $[Co(NO_2\text{-phen})_3]^{n+}$ ($E^0([Co(bpy)_3]^{n+})$ = 0.56 V vs NHE, $E^0([Co(NO_2\text{-phen})_3]^{n+})$ = 0.85 V vs NHE).[56] In our study, we used $[Co(bpy)_3]^{2+/3+}$ as a redox mediator. Therefore, reference DSSCs and plasmonic DSSCs showed V_{oc} around 0.7 V, consistent with previous reports.[57,58]

While V_{oc} and FF of plasmonic cells are similar to those of the reference cells, J_{sc} of the plasmonic DSSCs increased from 8.81 mA/cm^2 to 10.29 mA/cm^2. We also investigate LSPR effect on the photovoltaic performance of plasmonic DSSCs with thinner thickness. In Figure S2 and Table S2 in the Supporting Information, the plasmonic DSSCs with 1.1 μm also showed enhancement of J_{sc} and η, whereas V_{oc} and FF of plasmonic cells are similar to those of reference. Therefore, the obvious increase of J_{sc} is the predominant efficiency improvement factor through the LSPR effect on the light harvesting of dye molecules.

To further investigate the LSPR effect on the spectral response for DSSCs, an IPCE measurement was performed. The IPCE can be expressed by[59]

$$\mathrm{IPCE}(\lambda) = \mathrm{LHE}(\lambda)\varphi_{inj}\eta_{coll} \quad (4)$$

where LHE(λ) is the light-harvesting efficiency for photons at a given wavelength, ϕ_{inj} is the electron injection efficiency, and η_{coll} is the electron collection efficiency. The enhanced light absorption of the sensitized photoanodes by LSPR effect induces the light harvesting increase and consequently enhances the IPCE of solar cells. As expected, a higher IPCE value is observed for the plasmonic DSSC as shown in Figure 7a. Figure 7b represents the IPCE enhancement (%) of the plasmonic DSSCs employing 0.07 wt % Au NPs with respect to the reference cells. The IPCE enhancement is observed over the whole spectral range, and the degree of enhancement is more prominent in the range 600−700 nm. This observation is consistent with previous reports.[60,61] As shown in Figure S3 in the Supporting Information, Au NPs in TiO_2 photoanode sustain their size and shape after heat treatment because there is enough gap of space between Au NPs, avoiding Oswald ripening. We could conjecture that the size change of Au NPs were not a dominant factor of the tendencies of IPCE enhancement in our devices. Therefore, the IPCE enhancement tendencies could be due to the medium effect on LSPR peak wavelength (λ_{max}). As the refractive index of medium increases, λ_{max} shifts to longer wavelength.[62] The LSPR peak position of

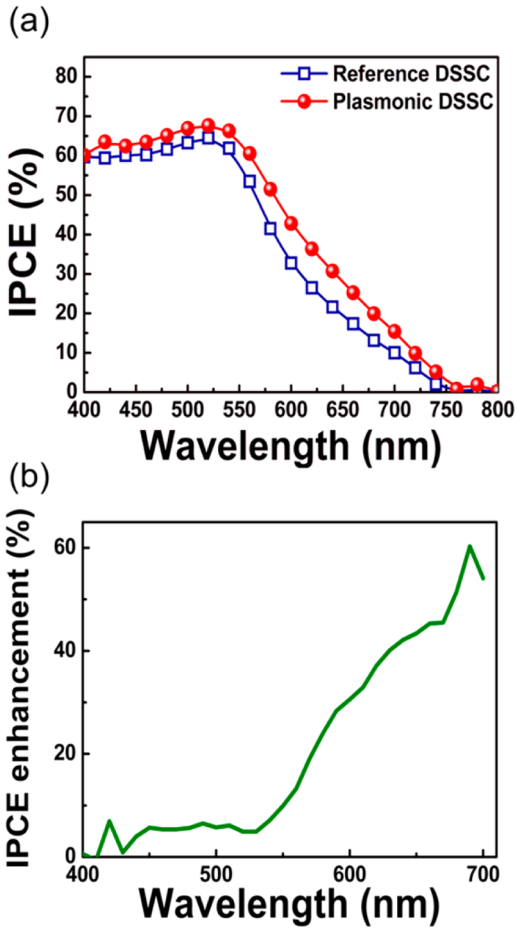

Figure 7. (a) Incident photon-to-current conversion efficiency (IPCE) spectra of the reference DSSCs with pristine TiO_2 photoanodes (blue line) and plasmonic DSSCs with 0.07 wt % Au NP-incorporated photoanodes (red line). (b) IPCE enhancement of plasmonic DSSCs with Au NPs, where the IPCE enhancement (%) = ($\mathrm{IPCE}_{\mathrm{plasmonic\ cell}}(\lambda)$ − $\mathrm{IPCE}_{\mathrm{reference\ cell}}(\lambda)$)/$\mathrm{IPCE}_{\mathrm{reference\ cell}}$ × 100.

Au NPs in anatase TiO_2 film is predicted at 648 nm according to Mie theory.[63] Thus, Au NPs embedded in anatase TiO_2 films of DSSCs could show red-shift in λ_{max} and the LSPR effect on the photovoltaic performance could increase in 600−700 nm. In the wavelength range over 700 nm, the IPCE enhancement could be due to the poor signal-to-noise ratio of IPCE measurement in longer wavelength spectrum.[60]

We also investigated the absorbed photon-to-current efficiency (APCE) for an in-depth investigation of the LSPR effect on the enhanced photovoltaic characteristics of DSSCs. The APCE is given by[64,65]

$$\begin{aligned}\mathrm{APCE} &= \frac{\mathrm{IPCE}(\lambda)}{\mathrm{LHE}(\lambda)} \\ &= \frac{\mathrm{IPCE}(\lambda)}{\alpha_{\mathrm{active\ layer}}} \\ &= \frac{\mathrm{IPCE}(\lambda)}{1 - R_{\mathrm{active\ layer}} - T_{\mathrm{active\ layer}}} \\ &= \varphi_{inj}\eta_{coll}\end{aligned} \quad (5)$$

where APCE is the product of $\phi_{inj}\eta_{coll}$. The LHE(λ) value which corresponds to the absorbance of active layer ($\alpha_{\mathrm{active\ layer}}$)

is increased by the localized enhanced electromagnetic field near the Au NPs. However, both ϕ_{inj} and η_{col} are not significantly affected by LSPR effect. Thus, there was no appreciable difference of APCE between reference and plasmonic cells.[66] To carry out a detailed analysis, we calculated the LHE(λ) of the electrodes by subtracting the difference between the transmittance of active layer ($T_{active\ layer}$) and the reflectance of active layer ($R_{active\ layer}$) from unity.[67] Using an integrating sphere, $T_{active\ layer}$ and $R_{active\ layer}$ were measured by UV−vis spectra. Figure 8a shows the APCE spectrum of the reference cells and plasmonic cells with 0.07 wt % Au NPs. The plasmonic cells show similar APCE values to the reference cells over the whole wavelength region. Although the IPCE of the plasmonic DSSCs increased over that of the reference cells, we found no distinction between the APCE of the plasmonic and reference cells. Therefore, the enhanced photocurrent of plasmonic DSSCs is predominantly determined by the improvement of LHE(λ) value via the LSPR effect. The APCE enhancement, shown in Figure 8b, indicates analogous APCE values over a wide spectral region. These results explicitly demonstrate that the enhanced light harvesting of dye molecules by localized electromagnetic fields near plasmonic NPs accounts for the improved photocurrent.

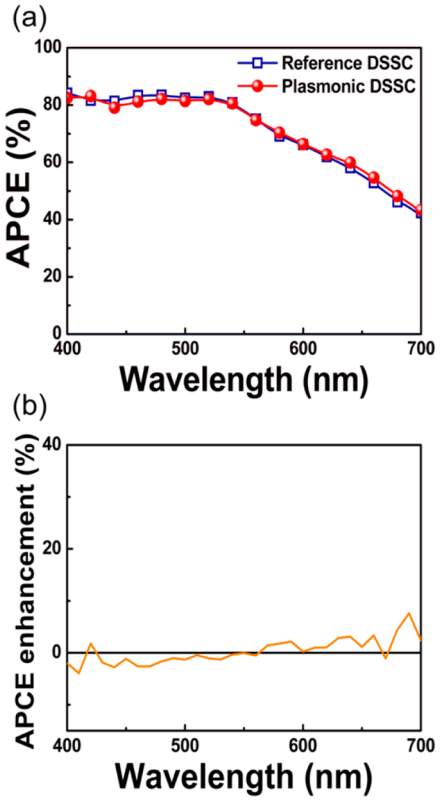

Figure 8. (a) Absorbed photon to current efficiency (APCE) of the reference DSSCs (red line) and plasmonic DSSCs with 0.07 wt % Au NPs (blue line). (b) APCE enhancement of plasmonic DSSCs with Au NPs, where the APCE enhancement (%) = ($APCE_{plasmonic\ cell}(\lambda)$ − $APCE_{reference\ cell}(\lambda)$)/$APCE_{reference\ cell}$ × 100.

Long-Term Stability of Plasmonic DSSCs with Cobalt-Based Electrolytes. The primary motivation of this work is to develop long-term stable plasmonic DSSCs by replacing the conventional iodine based electrolytes by cobalt based electrolytes. Thus, we monitored the performance change of DSSCs employing cobalt based electrolytes with time. Panels a and b in Figure 9 reveals J_{sc} and η for the plasmonic and reference devices with cobalt redox electrolyte for 1000 h. During the test, the photovoltaic properties of the cells were periodically measured, and the cells were stored under dark conditions at room temperature. As shown in Figure 9a and b, the plasmonic DSSCs maintained an improvement of J_{sc} and η by 17 and 11%, respectively, during the test. After 1000 h, the plasmonic DSSCs continue to exhibit superior performances over those of the reference cells due to the sustainable LSPR effects. These data correspond with the UV−vis and CV measurements in Figures 2 and 3. On the basis of our investigation, we can confirm long-lasting LSPR effects for increasing the light harvesting efficiency of DSSCs using a noncorrosive cobalt redox mediator.

CONCLUSIONS

In summary, we demonstrate that the LSPR effect can enhance the photovoltaic performance of DSSCs and the long-term stability of exquisite plasmonic structures using cobalt redox electrolytes. In order to precisely control the size of Au NPs, the Au NPs are synthesized using a phase transfer method with a DMAP stabilizer. This method is advantageous because uniformly sized Au NPs can be mass produced and easily applied to DSSCs photoanodes. The photovoltaic parameters are dependent on the concentration of Au NPs in TiO_2

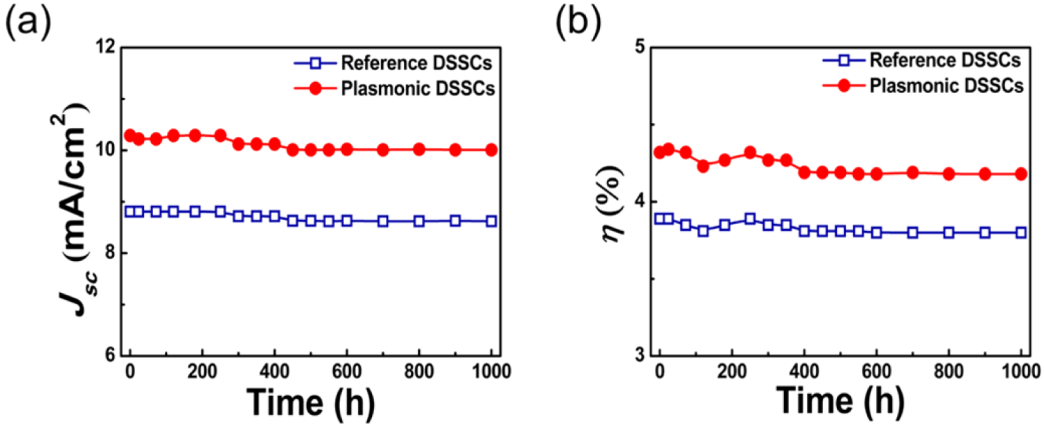

Figure 9. Long-term stability of the reference DSSCs (blue line) and plasmonic DSSCs (red line) with cobalt redox mediator. (a) Short circuit current density and (b) efficiency of cells using $[Co(bpy)_3]^{2+/3+}$ redox electrolytes.

photoanode. With 0.07 wt % Au NPs, the DSSCs exhibited preeminent cell performance among those incorporating various concentrations of Au NPs. Compared to the reference cells without Au NPs, the DSSCs incorporated with 0.07 wt % Au NPs showed improvements in J_{sc} and η by 17 and 11%, respectively, without considerable differences in V_{oc} and FF. This improvement of the photovoltaic performance is predominantly due to the enhanced optical absorption of the dye molecules as a result of the intensified electromagnetic field near the Au NPs. The LSPR effect on the photocurrent was further characterized by UV−vis, IPCE, and APCE analysis. Compared to the reference DSSCs, the IPCE and UV−vis spectra of plasmonic DSSCs showed enhanced light harvesting of dye molecules over the whole wavelength spectrum. However, there was no discernible difference in the APCE spectra between the plasmonic and reference DSSCs. Therefore, light harvesting improvement by LSPR effect was the primary factor in the enhanced photovoltaic performance of the DSSCs. The plasmonic DSSCs with cobalt redox mediator also exhibited improved stability of the Au nanostructures, compared to those with the I^-/I_3^- redox electrolyte. Using the $[Co(bpy)_3]^{2+/3+}$ redox electrolyte, the LSPR effects for the enhanced light harvesting of DSSCs could be maintained for 1000 h. This result verifies that cobalt complexes are promising materials for maximizing the performance of plasmonic DSSCs and the long-term stability of plasmonic structures. Therefore, our approach will lead the realization of highly reliable plasmonic DSSCs.

EXPERIMENTAL SECTION

Synthesis of Au NPs. The Au NPs were synthesized using a two-phase method based on ligand exchange reported by D. I. Gittins et al.[46] First, a 30 mL solution of aqueous gold chloride ($HAuCl_4$, 30 mM) was added to an 80 mL solution of tetraoctylammonium bromide in toluene (TOABr, 25 mM). After all Au precursors were transferred into the toluene phase, a 25 mL solution of sodium borohydride ($NaBH_4$, 0.4 M) was added to the stirred mixture. Then, the two phases in the mixture were separated, and the water phase was discarded. The prepared Au NPs in toluene phase were washed with 0.1 M H_2SO_4, 0.1 M NaOH, and H_2O. Finally, a 35 mL solution of 4-dimethylaminopyridine (DMAP, 0.1 M) in deionized (DI) water was added to the as-prepared TOABr-capped Au mixtures. The phase transfer across the interface of two phases finished within 10 h.

Characterization of Au NPs. Structures of Au NPs were examined by transmission electron microscopy (FEI, TECNAI G^2 F30 ST, at 100 kV). The X-ray diffraction (XRD) patterns of Au NPs were obtained by using an X-ray diffractometer (Rigaku, D/MAX-2500) equipped with a rotating anode and Cu K_α radiation source (λ = 0.15418 nm). The absorbance spectra of Au NPs were measured by an ultraviolet−visible (UV−vis) spectrophotometer (PerkinElmer, Lambda 35) in the wavelength range of 350−800 nm. The electrochemical activities of the Au-adsorbed fluorine-doped tin oxide (FTO) electrodes were investigated by an electrochemical analyzer (CH Instruments Inc., CH1600C) using a single-compartment cell equipped with the Au-coated FTO as a working electrode, a platinum (Pt) wire counter electrode, and an Ag/Ag^+ (0.1 M $AgNO_3$) reference electrode. In this case, the cyclic voltammograms (CV) curves of Au-coated FTO electrodes were obtained using different redox couples (I^-/I_3^- and $[Co(bpy)_3]^{2+/3+}$) at a scan rate of 25 mV/s. The cobalt redox electrolyte contained 0.22 M $[Co(bpy)_3](PF_6)_2$, 0.033 M $[Co(bpy)_3](PF_6)_3$, 0.1 M $LiClO_4$, and 0.2 M 4-*tert*-butylpyridine (TBP) in acetonitrile (ACN). The composition of the I^-/I_3^- redox electrolyte was an ACN solution containing 0.1 M $LiClO_4$, 0.05 M LiI, 0.03 M I_2, 0.1 M guanidinium thiocyanate (GSCN), and 0.5 M TBP.

Synthesis of Cobalt Complexes. The cobalt complexes $[Co(bpy)_3(PF_6)_2]^{2+}$ and $[Co(bpy)_3](PF_6)_2]^{3+}$ were synthesized using the following procedure.[68] The cobalt(II) chloride hexahydrate ($CoCl_2 \cdot 6H_2O$, 5 mmol) and 2,2′-bipyridyl (16.5 mmol) were dissolved in 30 mL of methanol and refluxed for 2 h. After cooling, ammonium hexfluorophosphate (NH_4PF_6, 25 mmol) was added to the reaction solution for precipitation. The precipitated compound was filtered and dried under vacuum. To obtain the cobalt(III) complex, we performed the oxidation of $[Co(bpy)_3(PF_6)_2]^{2+}$ by adding excess nitrosonium tetrafluoroborate ($NOBF_4$) to the cobalt(II) complex in the ACN solution. After removing the ACN with a rotary evaporator, we redissolved the residue in 20 mL of ACN, and an excess amount of $NOBF_4$ was added to the solution. The precipitated product was filtered and dried under vacuum.

Preparation of Solar Cells. A TiO_2 paste incorporating DMAP-capped Au NPs was fabricated with the following modified procedure.[33,34] Various amounts of Au NPs (Au to TiO_2 weight ratio from 0.03 to 0.1 wt %) were mixed with the TiO_2 paste (consisting of TiO_2, ethyl cellulose, lauric acid, and terpineol), followed by stirring and sonicating for 10 h. After mixing the TiO_2 paste with Au NPs, FTO glasses (TEC-8, Pilkington) were cleaned with an ethanol solution using sonication. Both the pristine TiO_2 paste and TiO_2 paste with Au NPs were coated on the FTO glasses using a doctor-blade, and the thickness of TiO_2 film was fixed at 4 μm. The deposited TiO_2 photoanodes were sintered at 500 °C for 30 min in air. Before the dye adsorption, the annealed TiO_2 electrodes were immersed in a $TiCl_4$ solution at 80 °C for 30 min and sintered again for 30 min. After $TiCl_4$ treatment, the TiO_2 photoanodes were immersed into 0.6 mM *cis*-Bis(isothiocyanato)(2,2′-bipyridyl-4,4′-dicarboxylato)(4,4′-dinonyl-2′-bipyridyl)ruthenium(II) (Z907 dye, Dyesol) in an ACN:*tert*-butyl alcohol (1:1 vol %) for 24 h. Then, the dyed photoanodes were rinsed with ethanol. For the counter electrodes, the FTO-coated glasses were cleaned with ethanol and coated with a 7 mM H_2PtCl_6 solution before they were sintered at 400 °C for 20 min. The counter electrodes and dyed photoanodes were assembled into a sandwich type cell and sealed with a spacer (25-μm-thick Surlyn, Solaronix). The electrolyte solutions based on I^-/I_3^- and $[Co(bpy)_3]^{2+/3+}$ were injected into a hole, which was drilled in the assembled cells, using capillary action. The cobalt redox mediator included 0.22 M $[Co(bpy)_3](PF_6)_2$, 0.033 M $[Co(bpy)_3](PF_6)_3$, 0.1 M $LiClO_4$ and 0.2 M 4-*tert*-butylpyridine in ACN. For comparison, the I^-/I_3^- redox electrolyte was prepared by an ACN solution containing 0.1 M $LiClO_4$, 0.05 M LiI, 0.03 M I_2, 0.1 M GSCN, and 0.5 M TBP.

Characterization of Solar Cells. The thickness of TiO_2 photoanodes was measured by a surface profiler (KLA-Tencor, Alpha-step IQ). The optical properties of the TiO_2 photoanodes and devices were measured by UV−vis spectrophotometer (PerkinElmer, Lambda 35) in the wavelength spectrum of 350−800 nm. The amounts of dye loading were measured by UV−vis spectra of the desorbed dye molecules using a 1 M NaOH aqueous solution. The photovoltaic properties of the solar cells were measured by a solar simulator equipped with a 1600 W xenon lamp (Yamashida Denso, YSS-200A) and a Keithley model 2400 source measurement unit. A solar simulator with a KG-3 filter served as the light source. A National Renewable Energy Laboratory (NREL)-calibrated Si solar cell was used as a reference cell to adapt the light intensity to AM 1.5G and the 1 sun condition. The active area for each cell was 0.40 cm^2, which was measured by a digital microscope camera (Moticam1000). Before the photocurrent density−voltage (J−V) measurement, a black aperture mask was attached on each cell to prevent additional illumination from lateral light. An incident photon-to-current conversion efficiency (IPCE) system (PV Measurements Inc.) was used to measure the IPCE as a function of the wavelength between 300 and 800 nm.

ASSOCIATED CONTENT

Supporting Information

Statistical analysis data of device performance parameters for reference DSSCs and plasmonic DSSCs, Photocurrent density−voltage (J−V) curves of reference DSSC and plasmonic DSSC with 1.1 μm photoanodes, TEM characterization of Au NPs in TiO_2 photoanode after sintering process.

This material is available free of charge via the Internet at http://pubs.acs.org.

AUTHOR INFORMATION

Corresponding Author

*E-mail: mjko@kist.re.kr. Tel.: +82-2-958-5518. Fax: +82-2-958-6649.

Author Contributions

†H.J. and B.K. contributed equally to this work

Notes

The authors declare no competing financial interest.

ACKNOWLEDGMENTS

This research was supported by the Global Frontier R&D Program on Center for Multiscale Energy System (2012M3A6A7054856) and 2014 University-Institute cooperation program funded by the National Research Foundation under the Ministry of Science, ICT & Future Planning, Korea; This work was also supported by the KIST institutional programs (2E24821 and Young Fellow Grant (2V03780)) and the "National Agenda Project" program of Korea Research Council of Fundamental Science & Technology (KRCF)

REFERENCES

(1) Faraday, M. The Bakerian Lecture: Experimental Relations of Gold (and Other Metals) to Light. *Philos. Trans. R. Soc. London* **1857**, *147*, 145−153.

(2) Jones, M. R.; Osberg, K. D.; Macfarlane, R. J.; Langille, M. R.; Mirkin, C. A. Templated Techniques for the Synthesis and Assembly of Plasmonic Nanostructures. *Chem. Rev.* **2011**, *111*, 3736−3827.

(3) Eustis, S.; El-Sayed, N. A. Why Gold Nanoparticles are more precious than Pretty Gold: Noble Metal Surface Plasmon Resonance and Its Enhancement of the Radiative and Nonradiative Properties of Nanocrystals of Different Shapes. *Chem. Soc. Rev.* **2006**, *35*, 209−217.

(4) Nabika, H.; Takase, M.; Nagasawa, F.; Murakoshi, K. Toward Plasmon-Induced Photoexcitation of Molecules. *J. Phys. Chem. Lett.* **2010**, *1*, 2470−2487.

(5) Koh, A. L.; Fernaindez-Domiinguez, A. I.; McComb, D.; Maier, S. A.; Yang, J. K. W. High-Resolution Mapping of Electron-Beam-Excited Plasmon Modes in Lithographically Defined Gold Nanostructures. *Nano Lett.* **2011**, *11*, 1323−1330.

(6) Slaughter, L.; Chang, W. S.; Link, S. Characterizing Plasmons in Nanoparticles and Their Assemblies with Single Particle Spectroscopy. *J. Phys. Chem. Lett.* **2011**, *2*, 2015−2023.

(7) Morton, S. M.; Silverstein, D. W.; Jensen, L. Theoretical Studies of Plasmonics using Electronic Structure Methods. *Chem. Rev.* **2011**, *111*, 3962−3994.

(8) Nie, S.; Emory, S. R. Probing Single Molecules and Single Nanoparticles by Surface-Enhanced Raman Scattering. *Science* **1997**, *275*, 1102−1106.

(9) Kneipp, K. Surface-Enhanced Raman Scattering. *Phys. Today* **2007**, *60*, 40−46.

(10) Fang, Y.; Seong, N. H.; Dlott, D. D. Measurement of the Distribution of Site Enhancements in Surface-Enhanced Raman Scattering. *Science* **2008**, *321*, 388−392.

(11) Knight, M. W.; Sobhani, H.; Nordlander, P.; Halas, N. J. Photodetection with Active Optical Antennas. *Science* **2011**, *332*, 702−704.

(12) Srituravanich, W.; Fang, N.; Sun, C.; Luo, Q.; Zhang, X. Plasmonic Nanolithography. *Nano Lett.* **2004**, *4*, 1085−1088.

(13) Liu, Z.; Hou, W.; Pavaskar, P.; Aykol, M.; Cronin, S. B. Plasmon Resonant Enhancement of Photocatalytic Water Splitting Under Visible Illumination. *Nano Lett.* **2011**, *11*, 1111−1116.

(14) Kamat, P. V. Photophysical, Photochemical and Photocatalytic Aspects of Metal Nanoparticles. *J. Phys. Chem. B* **2002**, *106*, 7729−7744.

(15) Subramanian, V.; Wolf, E. E.; Kamat, P. V. Catalysis with TiO_2/Gold Nanocomposites. Effect of Metal Particle Size on the Fermi Level Equilibration. *J. Am. Chem. Soc.* **2004**, *126*, 4943−4950.

(16) Jung, L. S.; Campbell, C. T.; Chinowsky, T. M.; Mar, M. N.; Yee, S. S. Quantitative Interpretation of the Response of Surface Plasmon Resonance Sensors to Adsorbed Films. *Langmuir* **1998**, *14*, 5636−5648.

(17) Brockman, J. M.; Nelson, B. P.; Corn, R. M. Surface Plasmon Resonance Imaging Measurements of Ultrathin Organic Films. *Annu. Rev. Phys. Chem.* **2000**, *51*, 41−63.

(18) Atwater, H. A.; Polman, A. Plasmonics for Improved Photovoltaic Devices. *Nat. Mater.* **2010**, *9*, 205−213.

(19) Schaadt, D. M.; Feng, B.; Yu, E. T. Enhanced Semiconductor Optical Absorption via Surface Plasmon Excitation in Metal Nanoparticles. *Appl. Phys. Lett.* **2005**, *86*, 063106.

(20) Derkacs, D.; Lim, S. H.; Matheu, P.; Mar, W.; Yu, E. T. Improved Performance of Amorphous Silicon Solar Cells via Scattering from Surface Plasmon Polaritons in Nearby Metallic Nanoparticles. *Appl. Phys. Lett.* **2006**, *89*, 093103.

(21) Pillai, S.; Catchpole, K. P.; Trupke, T.; Green, M. A. Direct Generation of Charge Carriers in c-Si Solar Cells Due to Embedded Nanoparticles. *J. Appl. Phys.* **2007**, *101*, 093105.

(22) Konda, R. B.; Mundle, R.; Mustafa, H.; Bamiduro, O.; Pradhan, A. K.; Roy, U. N.; Cui, Y.; Burger, A. Surface Plasmon Excitation via Au Nanoparticles in n-CdSe/ p-Si Heterojunction Diodes. *Appl. Phys. Lett.* **2007**, *91*, 19111.

(23) Wu, J.; Chen, F.; Hsiao, Y.; Chien, F.; Chen, P.; Kuo, C.; Huang, M. H.; Hsu, C. Surface Plasmonic Effects of Metallic Nanoparticles on the Performance of Polymer Bulk Heterojunction Solar Cells. *ACS Nano* **2011**, *5*, 959−967.

(24) Wang, D. H.; Park, K. H.; Seo, J. H.; Seifter, J.; Jeon, J. H.; Kim, J. K.; Park, J. H.; Park, O. O.; Heeger, A. J. Enhanced Power Conversion Efficiency in PCDTBT/PC_{70}BM Bulk Heterojunction Photovoltaic Devices with Embedded Silver Nanoparticle Clusters. *Adv. Eng. Mater.* **2011**, *1*, 766−770.

(25) Ihara, M.; Tanaka, K.; Sakaki, K.; Honma, I.; Yamada, K. Enhancement of the Absorption Coefficient of *cis*-$(NCS)_2$ Bis(2,2'-bipyridyl-4,4'-dicarboxylate)ruthenium(II) Dye in Dye-Sensitized Solar Cells by a Silver Island Film. *J. Phys. Chem. B* **1997**, *101*, 5153−5157.

(26) Jeong, N. C.; Prasittichai, C.; Hupp, J. Photocurrent Enhancement by Surface Plasmon Resonance of Silver Nanoparticles in Highly Porous Dye-Sensitized Solar Cells. *Langmuir* **2011**, *27*, 14609−14614.

(27) Ding, I.-K.; Zhu, J.; Cai, W.; Moon, S.-J.; Cai, N.; Wang, P.; Zakeeruddin, S. M.; Gratzel, M.; Brongersma, M. M. L.; Cui, Y.; McGehee, M. D. Plasmonic Dye-Sensitized Solar Cells. *Adv. Energy Mater.* **2011**, *1*, 52−57.

(28) Hou, W.; Pavaskar, P.; Liu, Z.; Theiss, J.; Aykol, M.; Cronin, S. B. Plasmon Resonant Enhancement of Dye-Sensitized Solar Cells. *Energy Environ. Sci.* **2011**, *4*, 4650−4655.

(29) Chang, S.; Li, Q.; Xiao, X.; Wong, K. Y.; Chen, T. Enhancement of Low Energy Sunlight Harvesting in Dye-Sensitized Solar Cells Using Plasmonic Gold Nanorods. *Energy Environ. Sci.* **2012**, *5*, 9444−9448.

(30) Zhang, X.; Liu, J.; Li, S.; Tan, X.; Yu, M.; Du, J. Bioinspired Synthesis of Ag@TiO_2 Plasmonic Nanocomposites to Enhance the Light Harvesting of Dye-Sensitized Solar Cells. *RSC Adv.* **2013**, *3*, 18587−18595.

(31) Standridge, D.; Schatz, G. C.; Hupp, J. T. Toward Plasmonic Solar Cells: Protection of Silver Nanoparticles via Atomic Layer Deposition of TiO_2. *Lagmuir* **2009**, *25*, 2596.

(32) Standridge, D.; Schatz, G. C.; Hupp, J. T. Distance Dependence of Plasmon-Enhanced Photocurrent in Dye-Sensitized Solar Cells. *J. Am. Chem. Soc.* **2009**, *131*, 8407−8409.

(33) Qi, J.; Dang, X.; Hammond, P. T.; Belcher, A. M. Highly Efficient Plasmon-Enhanced Dye-Sensitized Solar Cells through Metal@Oxide Core−Shell Nanostructure. *ACS Nano* **2011**, *5*, 7108−7116.

(34) Choi, H.; Chen, W. T.; Kamat, P. V. *Know Thy Nano Neighbor.* Plasmonic *versus* Electron Charging Effects of Metal Nanoparticles in Dye-Sensitized Solar Cells. *ACS Nano* **2012**, *6*, 4418−4427.
(35) Wooh, S.; Lee, Y.-G.; Tahir, M. N.; Song, D.; Meister, M.; Laquai, F.; Tremel, W.; Bisquert, J.; Kang, Y. S.; Char, K. Plasmon-Enhanced Photocurrent in Quasi-Solid-State Dye-Sensitized Solar Cells by the Inclusion of Gold/Silica Core−Shell Nanoparticles in a TiO_2 Photoanode. *J. Mater. Chem. A* **2013**, *1*, 12627−12634.
(36) Willets, K. A.; Van Duyne, R. P. Localized Surface Plasmon Resonance Spectroscopy and Sensing. *Annu. Rev. Phys. Chem.* **2007**, *58*, 267−297.
(37) Kelly, K. L.; Coronado, E.; Zhao, L. L.; Schatz, G. C. The Optical Properties of Metal Nanoparticles: The Influence of Size, Shape, and Dielectric Environment. *J. Phys. Chem. B* **2003**, *107*, 668−677.
(38) Wang, M.; Chamberland, N.; Breau, L.; Moser, J.-E.; Humphry-Baker, R.; Marsan, B.; Zakeeruddin, S. M.; Gratzel, M. An Organic Redox Electrolyte to Rival Triiodide/Iodide in Dye-Sensitized Solar Cells. *Nat. Chem.* **2010**, *2*, 385−389.
(39) Li, D.; Li, H.; Luo, Y.; Li, K.; Meng, Q.; Armand, M.; Chen, L. Non-Corrosive, Non-Absorbing Organic Redox Couple for Dye-Sensitized Solar Cells. *Adv. Funct. Mater.* **2010**, *20*, 3358−3365.
(40) Tian, H.; Jiang, X.; Yu, Z.; Kloo, L.; Hagfeldt, A.; Sun, L. Efficient Organic-Dye-Sensitized Solar Cells Based on an Iodine-Free Electrolyte. *Angew. Chem., Int. Ed.* **2010**, *49*, 7328−7331.
(41) Hattori, S.; Wada, Y.; Yanagida, S.; Fukuzumi, S. Blue Copper Model Complexes with Distorted Tetragonal Geometry Acting as Effective Electron-Transfer Mediators in Dye-Sensitized Solar Cells. *J. Am. Chem. Soc.* **2005**, *127*, 9648−9654.
(42) Daeneke, T.; Kwon, T.-H.; Holmes, A. B.; Duffy, N. W.; Bach, U.; Spiccia, L. High-Efficiency Dye-Sensitized Solar Cells with Ferrocene-based Electrolytes. *Nat. Chem.* **2011**, *3*, 211−215.
(43) Kim, H.-S.; Ko, S.-B.; Jang, I.-H.; Park, N.-G. Improvement of Mass Transport of the $[Co(bpy)_3]^{II/III}$ Redox Couple by Controlling Nanostructure of TiO_2 Films in Dye-Sensitized Solar Cells. *Chem. Commun.* **2011**, *47*, 12637−12639.
(44) Sapp, S. A.; Elliott, C. M.; Contado, C.; Caramori, S.; Bignozzi, C. A. Substituted Polypyridine Complexes of Cobalt(II/III) as Efficient Electron-Transfer Mediators in Dye-Sensitized Solar Cells. *J. Am. Chem. Soc.* **2002**, *124*, 11215−11222.
(45) Nusbaumer, H.; Moser, J.-E.; Zakeeruddin, S. M.; Nazeeruddin, M. K.; Gratzel, M. $Co^{II}(dbbip)_2^{2+}$ Complex Rivals Tri-iodide/Iodide Redox Mediator in Dye-Sensitized Photovoltaic Cells. *J. Phys. Chem. C* **2001**, *105*, 10461−10464.
(46) Gittins, D. I.; Caruso, F. Spontaneous Phase Transfer of Nanoparticulate Metals from Organic to Aqueous Media. *Angew. Chem., Int. Ed.* **2001**, *16*, 3001−3004.
(47) Cai, W.; Wan, L.; Noda, H.; Hibino, Y.; Ataka, K.; Osawa, M. Orientational Phase Transition in a Pyridine Adlayer on Gold(111) in Aqueous Solution Studied by in Situ Infrared Spectroscopy and Scanning Tunneling Microscopy. *Langmuir* **1998**, *14*, 6992−6998.
(48) Mulvaney, P. Surface Plasmon Spectroscopy of Nanosized Metal Particles. *Langmuir* **1996**, *12*, 788−800.
(49) Brown, M. D.; Suteewong, T.; Kumar, R. S. S.; D'Innocenzo, V.; Petrozza, A.; Lee, M. M.; Wiesner, U.; Snaith, H. J. Plasmonic Dye-Sensitized Solar Cells Using Core−Shell Metal−Insulator Nanoparticles. *Nano Lett.* **2011**, *11*, 438−445.
(50) Nakao, Y.; Soneb, K. Reversible Dissolution/Deposition of Gold in Iodine-Iodide-Acetonitrile Systems. *Chem. Commun.* **1996**, 897−898.
(51) Qi, P. H.; Hiskey, J. B. Dissolution Kinetics of Gold in Iodide Solutions. *Hydrometallurgy* **1991**, *27*, 47−62.
(52) Alvarez-Puebla, R.; Liz-Marzan, L. M.; Garcia de Abajo, F. J. Light Concentration at the Nanometer Scale. *J. Phys. Chem. Lett.* **2010**, *1*, 2428−2434.
(53) Blaber, M. G.; Henry, A.-I.; Bingham, J. M.; Schatz, G. C.; Duyne, R. P. V. LSPR Imaging of Silver Triangular Nanoprisms: Correlating Scattering with Structure Using Electrodynamics for Plasmon Lifetime Analysis. *J. Phys. Chem. C* **2012**, *116*, 393−403.
(54) Noguez, C. Surface Plasmons on Metal Nanoparticles: The Influence of Shape and Physical Environment. *J. Phys. Chem. C* **2007**, *111*, 3806−3819.
(55) Chen, H.; McMahon, J. M.; Ratner, M. A.; Schatz, G. C. Computational Modeling of Plasmon-Enhanced Light Absorption in a Multicomponent Dye Sensitized Solar Cell. *J. Phys. Chem. C* **2010**, *114*, 10215−10221.
(56) Feldt, S. M.; Wang, G.; Boschloo, G.; Hagfeldt, A. Effect of Driving Forces for Recombination and Regeneration on the Photovoltaic Performance of Dye-Sensitized Solar Cells using Cobalt Polypyridine Redox Couples. *J. Phys. Chem. C* **2011**, *115*, 21500−21507.
(57) Mosconi, E.; Yum, J.-H.; Kessler, F.; Garcia, C. J. G.; Zuccaccia, C.; Cinti, A.; Nazeeruddin, M. K.; Gratzel, M.; Angelis, F. D. Cobalt Electrolyte/Dye Interactions in Dye-Sensitized Solar Cells: A Combined Computational and Experimental Study. *J. Am. Chem. Soc.* **2012**, *134*, 19438−19453.
(58) Liu, Y.; Jennings, J. R.; Huang, Y.; Wang, Q.; Zakeeruddin, S. M.; Gratzel, M. Cobalt Redox Mediators for Ruthenium-Based Dye-Sensitized Solar Cells: A Combined Impendance Spectroscopy and Near-IR Transmittance Study. *J. Phys. Chem. C* **2011**, *115*, 18847−18855.
(59) Gratzel, M. Solar Energy Conversion by Dye-Sensitized Photovoltaic Cells. *Inorg. Chem.* **2005**, *44*, 6841−6851.
(60) Jang, Y. H.; Jang, Y. J.; Kochuveedu, S. T.; Byun, M.; Lin, Z.; Kim, D. H. Plasmonic Dye-Sensitized Solar Cells Incorporated with Au-TiO_2 Nanostructures with Tailored Configurations. *Nanoscale* **2014**, *6*, 1823−1832.
(61) Nahm, C.; Choi, H.; Kim, J.; Jung, D.-R.; Kim, C.; Moon, J.; Lee, B.; Park, B. The Effects of 100 nm-Diameter Au Nanoparticles on Dye-Sensitized Solar Cells. *Appl. Phys. Lett.* **2011**, *99*, 253107.
(62) McFarland, A. D.; Duyne, R. P. V. Single Silver Nanoparticles as Real-Time Optical Sensors with Zeptomole Sensitivity. *Nano Lett.* **2003**, *3*, 1057−1062.
(63) Buso, D.; Pacifico, J.; Martucci, A.; Mulvaney, P. Gold-Nanoparticle-Doped TiO_2 Semiconductor Thin Films: Optical Characterization. *Adv. Funct. Mater.* **2007**, *17*, 347−354.
(64) Fillinger, A.; Parkinson, B. A. The Adsorption Behavior of a Ruthenium-Based Sensitizing Dye to Nanocrystalline TiO_2 Coverage Effects on the External and Internal Sensitization Quantum Yields. *J. Electrochem. Soc.* **1999**, *16*, 4559−4564.
(65) Hamann, T. W.; Jenson, R. A.; Martinson, A. B. F.; Ryswyk, H. V.; Hupp, J. T. Advancing Beyond Current Generation Dye-Sensitized Solar Cells. *Energy Environ. Sci.* **2008**, *1*, 66−78.
(66) Baek, S.-W.; Noh, J.; Lee, C.-H.; Kim, B.; Seo, M.-K.; Lee, J.-Y. Plasmonic Forward Scattering Effect in Organic Solar Cells: A Powerful Optical Engineering Method. *Sci. Rep.* **2013**, *3*, 1726.
(67) Ghadiri, E.; Tagavinia, N.; Zakeeruddin, S. M.; Gratzel, M.; Moser, J.-E. Enhanced Electron Collection Efficiency in Dye-Sensitized Solar Cells Based on Nanostructured TiO_2 Hollow Fibers. *Nano Lett.* **2010**, *10*, 1632−1638.
(68) Feldt, S. M.; Gibson, E. A.; Gabrielsson, E.; Sun, L.; Boschloo, G.; Hagfeldt, A. Design of Organic Dyes and Cobalt Polypyridine Redox Mediators for High-Efficiency Dye-Sensitized Solar Cells. *J. Am. Chem. Soc.* **2010**, *132*, 16714−16724.